ACS SENSORS

pubs.acs.org/acssensors
Article

Artificial Intelligence-Supported Colorimetric Multibiomarker Sensor to Enable Critical Neonatal Monitoring

Alejandra Castelblanco,[†] Elisabetta Ruggeri,[†] Giusy Matzeu, Motaharehsadat Heydarian, Kai Foerster, Ahmed Bahnasy, Andreas Flemmer, Julia A. Schnabel, Benjamin Schubert,* Fiorenzo G. Omenetto,* and Anne Hilgendorff*

Cite This: https://doi.org/10.1021/acssensors.5c04171

ABSTRACT: Clinical monitoring in the most vulnerable patients, such as newborns, relies on invasive and costly procedures and/or wired sensor surveillance, increasing discomfort and risk for undetected events. Addressing this critical need, we present a noninvasive, AI-supported multibiomarker monitoring sensor capturing multiple critical body functions via colorimetric analysis of body fluids. The sensor is optimized for its use in critically ill preterm neonates, where transepidermal fluid mirrors the interstitial compartment, thereby opening new avenues for future clinical monitoring. The silk-based sensor introduces twelve different colorimetric inks that stabilize labile bioresponsive molecules to a simple, wax-printed paper microfluidic wearable patch to facilitate real-time tracking of biomarkers (temperature (T), pH, sodium (S), and glucose (G)) on a miniaturized surface. Colorimetric responses showed high precision and reproducibility in sensing ranges relevant for neonatal care (T: 32−41 [°C]; pH: 3−9; S: 2.92−29.20 [mg/mL], G: 0.039−0.625 [mg/mL]). Deep learning for color response quantification achieved high-precision estimates (T: 0.455 [°C]; pH: 0.416; S: 0.857 [mg/mL], G:0.019 [mg/mL]; mean absolute error). The sensor's optimized interface for sample collection on skin and its performance under clinically relevant conditions, e.g., increased humidity (80%), tracking on moving object (0.986 AP@IoU = 0.5), sensor shear/rotation, uncontrolled light, as well as successful capture of physiological effects in biological fluids together with its miniaturized design caters to the critical needs of intensified monitoring in high-end patient populations such as neonates.

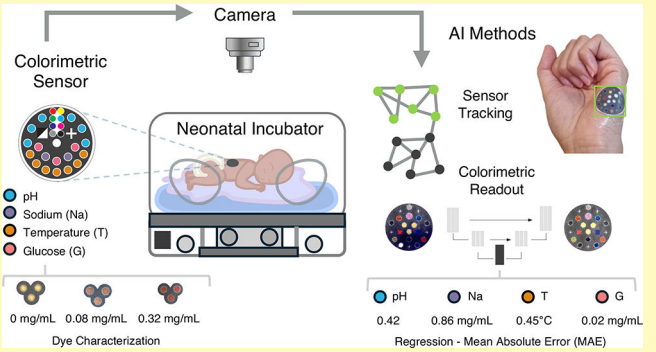

KEYWORDS: *wearable skin sensors, colorimetric sensors, AI colorimetric readout, newborn biomarker, computer vision newborns, neonatal incubator, noninvasive monitoring, biofluid, transepidermal fluid*

Monitoring critical functions of the human body with easy-to-use, wearable biofluid sensors that are carefully adapted to the critical needs of specific patient populations will revolutionize patient care as their application reduces the need for invasive procedures, extensive laboratory equipment, and costly production. The most challenging showcase for the design of such devices is their application to neonates after at-risk birth, as they require parallel monitoring of different body function biomarkers through miniaturized devices, ensuring skin conformability, biocompatibility, and clinical usability while reducing production costs or troublesome maintenance.

As of today, however, neonatal care depends on a comprehensive set of medical devices and laboratory tests to assess vital signs and metabolic (e.g., glucose/electrolyte homeostasis) as well as organ function (e.g., liver, kidney, heart) for the prevention of (undetected) complications and timely treatment decisions. Devices for nontraumatic, continuous monitoring in these patients are only available for distinct parameters such as blood oxygenation and temperature.[1,2] These devices are wire-dependent and exclude assessment of other relevant metabolic functions, thus increasing the risk for undetected electrolyte and glucose imbalances,[3−6] as well as increasing the delayed diagnosis of organ dysfunction (e.g., cystic fibrosis, liver failure).[6,7] Not only is the use of wired sensors in neonatal intensive care known to obstruct daily care tasks and reduce parental skin bonding,[8] but the subsequent need for invasive procedures also results in limitations for health care and trauma for the newborn and its family. Blood extractions are limited by sample volume and number as they

Received: November 6, 2025
Revised: May 18, 2026
Accepted: May 19, 2026

https://doi.org/10.1021/acssensors.5c04171
ACS Sens. XXXX, XXX, XXX-XXX

require painful vessel punctures, increase the risk of critical blood loss, infection, and employ costly laboratory analysis.[1,6,9,10]

Easily accessible body fluids such as perspiration and saliva remain largely unexplored for clinical, noninvasive health monitoring in pediatric patients.[10] One of the few examples is iontophoresis, where perspiration fluid is used for diagnostic purposes in infants with cystic fibrosis. Although successfully implemented in routine care, chemical sample analysis still requires laboratory equipment and holds the risk of skin irritation due to electric stimulation.[10] Likewise, continuous neonatal glucose monitoring in interstitial fluid, via subcutaneous biosensors, has shown improved glucose level control in clinical studies, with remaining risks of subcutaneous inflammation, needle insertion pain, sensor drift, and recalibration requirements.[4] Making biological fluids even more valuable for diagnostic strategies, transdermal fluid in the preterm neonate in part reflects the interstitial and circulatory compartment,[11] as skin immaturity increases insensible water loss, reaching up to permeation rates of 15−22 g/m^2/h.[12,13] In adults, *in situ* perspiration analysis through potentiometry or amperometry has been explored, although it is limited by the reliance of these tools on energy harvesting modules, low device flexibility, higher weight, and significant maintenance, restricting their application in routine clinical care.[14,15]

The possibility to advance clinical care by the use of high-end inventions in the bioengineering field was only taken up in a few devices that explored the use of microfluidic structures for passive biological fluid collection and chemical analysis,[16,17] including polymeric or paper-based colorimetric sensors.[18−22] The use of flexible and absorbent materials is crucial to ensure effective fluid sampling while avoiding skin irritation through traction. Not yet meeting clinical needs, especially in critical patient populations, previous studies have mainly focused on detecting single analytes, and only a few studies have focused on colorimetric wearable multibiomarker, sensing[23−26] or longitudinal sampling.[27] No studies, however, have successfully adapted the sensor in function and design to the specific challenges of neonatal monitoring, thereby missing opportunities that noninvasive, lightweight paper-based colorimetric sensing devices can offer for critical patient populations.

Adding to the complexity of the clinical solution needed, current colorimetric sensors are often limited by relying on human visual interpretation, which, influenced by illumination conditions and the visual acuity of the examiner, can result in significant measurement errors.[28,29] Therefore, artificial intelligence (AI)-based image analysis and robust colorimetric signal digitalization[30,31] represent a promising alternative for standardized, objective, and automated neonatal monitoring in the clinic, thereby alleviating the workload of nurses and other healthcare professionals. Advanced AI models are needed to integrate challenges posed by uncontrolled light conditions in the clinical setting, as well as demonstrate efficacy for tracking the sensor on a moving patient, as minimal handling and free range of motion for the patient is desired in pediatrics and especially neonatal care.

To address the clinical need for noninvasive, wireless monitoring of health indicators in the challenging conditions brought forward in critically ill neonates, we developed miniaturized microfluidic silk-based colorimetric sensors and combined them with a deep-learning imaging system to enable the noninvasive measurement of multiple critical physiological parameters in perspiration fluid, accompanied by demonstrating its alternative use in saliva (Figure 1). For neonatal monitoring, we achieved measurements of biomarkers that reflect critical functions in four different categories: (1) temperature as an example for critical body function, (2) glucose for energy consumption, (3) pH for metabolic balance, and (4) sodium for fluid balance/electrolyte homeostasis in clinically relevant ranges. To improve sensing reliability, we tested different chromogenic compounds for each analyte. Furthermore, accurate digital colorimetric analysis was achieved with our deep-learning imaging pipeline, even in uncontrolled light conditions. Working towards direct clinical application, key aspects of clinical feasibility, including microfluidic performance, dye stability in the neonatal incubator, and experimental application with biological fluids, were investigated, demonstrating the sensor's potential for future clinical application.

MATERIALS AND METHODS

Sensor Fabrication and Design

Silk Fibroin Solution Preparation. Silk fibroin was extracted following a previously described protocol.[21] In summary, finely chopped *Bombyx mori* silk cocoons were boiled in a solution of 0.02 M sodium carbonate to remove the sericin layer for 120 min. The fibers were washed three times for 20 min in DI water, dried for 10 h, and dissolved in a solution of lithium bromide 9.3 M at 60 °C for 4 h. The resulting solution was dialyzed against deionized water for 2 days, changing the deionized water 6 times at consistent intervals. The solution was centrifuged twice at a speed of 9000 rpm, at 4 °C, for 20 min and then filtered, yielding 7−8 wt % silk fibroin solution.

Chromogenic Enzymatic Glucose-Sensing Areas. Silk-based chromogenic enzymatic inks were prepared using 4 wt % silk fibroin solutions containing 0.1 M PBS to maintain a stable pH when reacting with strongly acidic or basic sweat. Enzymatic reagents were added to the silk solution at final concentrations of 339 U mL^{-1} for Peroxidase from horseradish Type I (HRP) and 645 U mL^{-1} for glucose oxidase (GOx). Chromogenic substrates were then dissolved in the silk-based enzymatic mixture to yield final concentrations of 0.75 mg mL^{-1} of 4-aminoantipyrine, 0.3 mg mL^{-1} of acid yellow 34, and 1.7 mg mL^{-1} of sodium 3,5-dichloro-2-hydroxybenzenesulfonate. The circular sensing areas were first functionalized with 0.4 μL of a chitosan solution consisting of 0.5 wt % chitosan dissolved in 2 wt % acetic acid, which was allowed to dry at room temperature. Subsequently, 0.4 μL of the chromogenic enzymatic ink was drop-cast onto the chitosan layer and allowed to dry at room temperature. This deposition process of the silk-based ink was repeated four times to obtain a total of four layers of ink.

Chromogenic pH-Sensing Areas. Silk-based chromogenic pH-sensitive inks were made of 4 wt % silk fibroin solutions containing three different pH indicators (i.e., phenol red sodium salt, nitrazine yellow, bromocresol green sodium salt) with a final concentration of 2.5 mg mL^{-1}. 0.3 μL of the ink was drop-cast on the circular areas. The inks were dried at room temperature, and the process was repeated a second time to obtain 2 layers of ink.

Chromogenic Temperature-Sensing Areas. Temperature-sensitive inks were made of 65 wt % DI water, 32.5 wt % Mod Podge, and 2.5% thermochromic pigment (Atlanta Chemical, USA). 0.5 μL of the ink was drop-cast on the circular areas. The ink was let dry at room temperature, and the process was repeated a second time to obtain 2 layers of ink.

Chromogenic Sodium-Sensing Areas. A sodium-sensing ink was prepared consisting of chromoionophore I (0.06 wt %), sodium ionophore X (0.12 wt %), potassium tetrakis (4-chlorophenyl)borate (0.11 wt %), poly(vinyl chloride) (0.86 wt %), bis(2-ethylhexyl) sebacate (3.43 wt%), and tetrahydrofuran (95.41 wt %). The mixture was prepared by sequential addition of the components and stirred

https://doi.org/10.1021/acssensors.5c04171
ACS Sens. XXXX, XXX, XXX-XXX

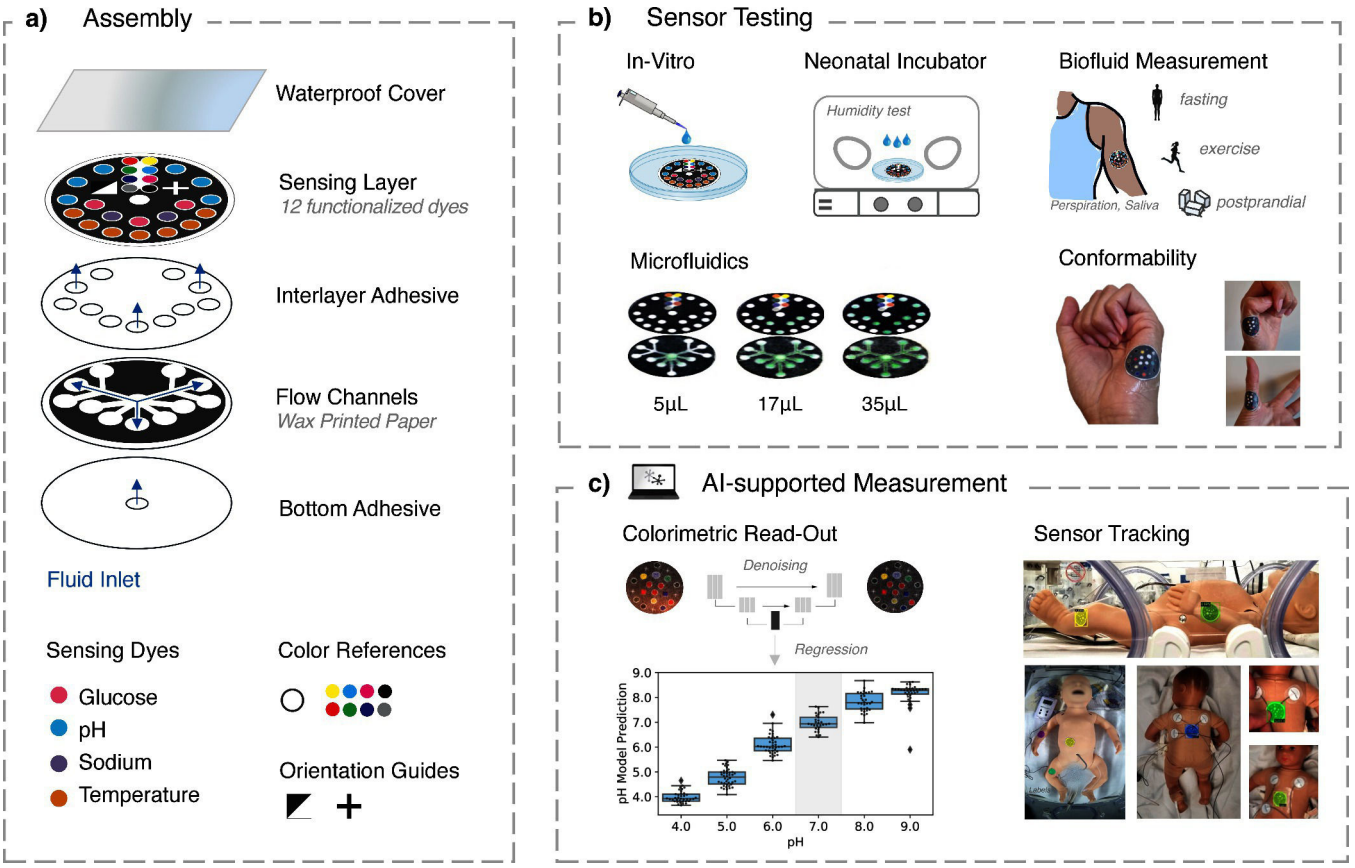

Figure 1. Colorimetric silk-based sensor for multibiomarker detection in biological fluids, integrated with artificial intelligence (AI) for parameter readout and targeted for physiological monitoring in neonatal care. (A) Schematic of the sensor assembly, the first sensing layer displays the colorimetric dyes, the intermediate layer contains multiple fluid flow channels, and the bottom layer allows fluid inlet. On top, a waterproof medical skin cover film improves dye stability and skin adhesion. (B) Colorimetric dye responses were characterized through multiple *in vitro* experiments. The sensor's technical feasibility was tested in the high-humidity conditions of the neonatal incubator and assessed for microfluidic functionality and skin conformability. Pilot experiments with biofluids evaluated the sensor's response under physiological variations. (C) AI-supported measurement was achieved by a new U-Net denoising model for colorimetric multivariate parameter regression (left), and a computer vision model for sensor tracking in the incubator (right).

overnight before use. The circular sensing areas were first functionalized with 0.7 µL of a 4 wt % silk solution, which was allowed to dry at room temperature, followed by 1 µL of 4 wt % silk solution to form a two-layer base. After drying, 0.1 µL of the sensing ink solution was drop-cast seven times onto each circular area on top of the silk base layer. A second 4 wt % silk fibroin solution was then applied as a capping layer by drop-casting 1 µL followed by 1.5 µL on top of the membrane layer.

Before assembling the patch, a buffer was added to the circular areas in correspondence with the sodium-sensing regions on the first paper layer of the patch that contains the flow channels. The buffer was prepared using 1 M HEPES solution adjusted to pH 6.89 (target range 6.85−6.95) by titration with 10 M KOH. 0.5 µL of the buffer solution was drop-cast five times on the circular areas to complete the intermediate buffering layer.

The manufacturing specifications of individual materials can be found in Supporting Text - Sensor Fabrication and Design.

Sensor Fabrication. Whatman Grade 1 filter paper was used as a substrate to fabricate the paper-based sensors. A vector graphic software (Adobe Illustrator) was employed to design the distribution pattern of the sensing areas and the fluidic flow channels. The wax pattern was printed directly onto the filter paper using a wax printer (Xerox ColorQube 8570). Afterwards, the wax-printed paper was heated at 150 °C for 30 s to allow the wax to melt and penetrate into the filter paper to create a hydrophobic channel pattern.

In Vitro Validation

The colorimetric response of silk-fibroin sensors was experimentally validated *in vitro* with specialized experimental setups (n = 34) under white-light conditions.

Temperature Calibration. Video recordings were acquired using an ultra-low-light 4K camera (*Sony STARVIS IMX415 CMOS*; 30 fps) mounted on a NVIDIA Jetson Xavier NX. Three sensors were attached between impermeable Tegaderm films, fixed to the inner wall of a glass container filled with water, and recorded while temperature was increased from 31 °C to 42 °C in 0.2 °C steps at 1 min intervals, followed by cooling from 42 °C to 30 °C to assess hysteresis (n = 3) (Figure S8b).

pH Calibration. Two sensors were recorded during cyclic exposure to pH 3−9 solutions (1 pH unit every 5 min) using incremental addition of HCl or NaOH under continuous stirring, with real-time monitoring by a pH meter (Figure S8c). Reverse cycling (pH 9 to 3) revealed a 28% color saturation loss due to prolonged submersion without waterproof covering. Additionally, seven sensors were recorded after application of 3 µL droplets at pH 3−9, in steps of 1 pH unit, to the bottom inlet of the pH sensing area.

Sodium Calibration. Images of (n = 11) sensors were captured while applying 3 µL standard solutions containing 50, 100, 130, 140, 150, 180, 200, 300, 500, 700, and 1000 mmol/L sodium chloride (NaCl) to the bottom inlet of the sodium sensing area.

https://doi.org/10.1021/acssensors.5c04171
ACS Sens. XXXX, XXX, XXX-XXX

Glucose Calibration. The colorimetric response for glucose was evaluated from pictures of (n = 8) sensors exposed to 2 μL of solutions with decreasing concentrations of glucose, following a serial dilution protocol. The glucose concentrations were 10, 5, 2.5, 1.25, 0.625, 0.3125, 0.1563, 0.078 mg/mL, and distilled water.

All images were white-balanced and grayscale-normalized using color checker references and GIMP 2.10. We developed a computational imaging pipeline to automatically localize, segment, and quantify sensor regions (Figure S8a). Sensitivity was calculated from the linear slope of the effective sensing range in each calibration curve.

Deep Learning Imaging Methods

Pipeline for Experimental Data Augmentation. Images of the sensors under white light (scene illuminated with LED 4500K) were used to capture the pixel color distributions for each of the variables (Figures S5−S7). Pictures of multiple sensor skeletons (n = 20) were obtained from the experimental *in vitro* validations, and sensing areas were masked. Random pixels from the experimental color distributions were sampled into the corresponding sensing areas of a sensor skeleton, generating augmented sensor images that contain all the measured parameters (pH, temperature, glucose, sodium) at randomly sampled levels. Illumination noise, random rotations, cropping, and shearing were applied to augment the images (Supporting Text - Deep Learning Imaging Methods).

Colorimetric Parameter Reading: Baseline Model. Estimation of parameters from the sensor images under reference white light was first performed with a baseline deep learning model for every variable, consisting of a convolutional neural network (CNN) coupled with a multilayer perceptron (MLP). The model input consisted of the RGB sensor image and a mask of the target sensing areas, with an input size of (128,128,4). The ground truth label was the corresponding variable value, min-max normalized in the measured range from [0−1] (Table S3).

Colorimetric Parameter Reading and Color Correction: U-Net Denoising Model. Estimation of the parameters from sensor images under varying nonuniform illumination noise, was achieved using newly developed denoising autoencoders based on the U-Net model[32] coupled with MLPs to perform regression for each variable from the latent features, thus integrating both the color correction and parameter inference tasks into a single framework (Figure 3a; Supporting Text - Deep Learning Imaging Methods; Table S4).

Sensor Segmentation in the Incubator. An instance segmentation model using a *Mask R-CNN* model with a feature pyramid network (FPN),[32,33] was trained for real-time detection of the newborn wearable sensors in the neonatal incubator conditions (Supporting Text - Deep Learning, Table S5).

Statistical Analysis. Statistical analyses were performed with Python 3.8.8 and SciPy 1.10.1. Statistical significance was assumed at $p < 0.05$.

Pilot Pre-Clinical Experiments

Sensor Detection in the Neonatal Incubator. Videos were recorded in a neonatal incubator (*Giraffe OmniBed, GE Healthcare*) at the Perinatal Center, LMU Hospital Munich, using sensors attached to the chest, back, arm, and/or leg of two neonatal mannequins (Figure S9). One mannequin (*SimNewB, LaerdalMedical, Puchheim, Germany*) simulated respiration (30−90 breaths/min) and automated limb motion, while the second was repositioned manually. An embedded camera system (*NVIDIA Jetson Xavier NX, e-CAM80_CUNX 8 MP*) was mounted above the incubator, with a smartphone camera (*12MP/64MP, Samsung Galaxy S21*) positioned laterally. The dataset comprised 31 videos (30−180 s) acquired under varying illumination (LED, daylight, low light with blanket cover) and conditions encountered in the clinic (i.e., cardiac electrodes attached, hands of clinical staff, partial occlusion of the sensor with bed sheets, reflections from a plastic cover; Table S2). Videos were subsampled, and a total of 655 frames (15−25 per video) were manually annotated by six trained researchers using *LabelMe*[34] for semantic segmentation.

Dye Stability in Incubator. Sensor dye stability was assessed at 80% humidity and 37−39 °C. An alkaline solution (pH 9) was applied to cotton pads (500 or 1000 μL), onto which sensors (n = 4) were placed, with two sensors having a waterproof film and the other two not. Sensors were recorded for 120 min using the incubator-mounted camera; temperature and humidity were independently monitored (Figure S8d). Color values were extracted using the computational video processing pipeline (Figure S8a).

Evaluation with Biological Fluids. Saliva and perspiration samples were collected from a healthy adult female under four conditions (fasting, post-exercise, 10 and 25 min post-prandial). Fluid samples were obtained through the CPC-M bioArchive at the Comprehensive Pneumology Center Munich. The study was approved by the local ethics committee of the Ludwig-Maximilians University of Munich, Germany (Ethic vote #19-629). Written informed consent was obtained from the study participant. Saliva (1 mL) was used for glucose sensing and validated by ELISA and capillary blood glucose measurement (*ACCU-check Performa, CE 0088, Roche*), while perspiration (0.5 mL) collected post-exercise was used for pH sensing and validated by laboratory pH meter (*WTW inoLab pH 720*). Colorimetric sensor measurements were performed using 3 μL sample volumes and imaged under daylight with a smartphone (*12MP/64MP, Samsung Galaxy S21*) and a color checker. In parallel, glucose levels in an aliquot of the biological fluid sample were measured by ELISA (*reference EIAGLUC, standard glucose range 0.5−32 mg/dL, Thermo Fisher, Invitrogen*) using a microplate laboratory spectrometer (*SpectraMax i3x, Molecular Devices*) and quantified from triplicate measurements via polynomial fitting of manufacturer standards.

RESULTS

Colorimetric Sensing Technology and Experimental Characterization

The sensor patch is constructed from biocompatible silk-fibroin (diameter 2.8 cm, thickness ∼0.2 mm, weight 0.05 g) and mounted on a detachable Tegaderm film to minimize skin discomfort (Figure 1a). A laser-cut circular inlet (3 mm) enables fluid entry into the sensor. Following the base layer, an intermediate wax-printed paper layer with ramified microfluidic channels for sample distribution, and a top wax-printed layer containing sensing areas and color reference markers, are laminated using adhesive films. A transparent, water-resistant, medically approved adhesive film covers the sensor to prevent leakage and contamination. Twelve distinct colorimetric dyes are printed in individual circular regions, including seven temperature, three pH, one glucose, and one sodium dye; dyes are based on biocompatible silk and chitosan matrices combined with enzymes (e.g., glucose oxidase and horseradish peroxidase) and indicator pigments to generate target-specific colorimetric responses.

In extensive *in vitro* experiments, the color response was recorded upon exposure to specific target concentrations in standard solutions or controlled temperature conditions, respectively, using clinically relevant ranges for each parameter (Table S1). Color values were extracted through image analysis to generate calibration curves and to determine the dyes' sensitivity and effective sensing range.

For *temperature* measurements, the sensitivity, quantified as grayscale response [0−1] per °C, and the sensing range were measured for the seven colorimetric dyes (Figure 2a,c; Figure S2a): T1 (0.194, 33−36 °C), T2 (0.140, 35−38 °C), T3 (0.064, 32−41 °C), T4 (0.070, 35.5−41 °C), T5 (0.046, 36−41 °C), T6 (0.137, 32−35.5 °C, and 0.040, 36−41 °C), T7 (0.032, 37−40 °C), with the integrated response of all dyes enabling measurements in the range from 32 °C to 41 °C. The color response was reproducible in simultaneous measurements with three different sensors;

https://doi.org/10.1021/acssensors.5c04171
ACS Sens. XXXX, XXX, XXX-XXX

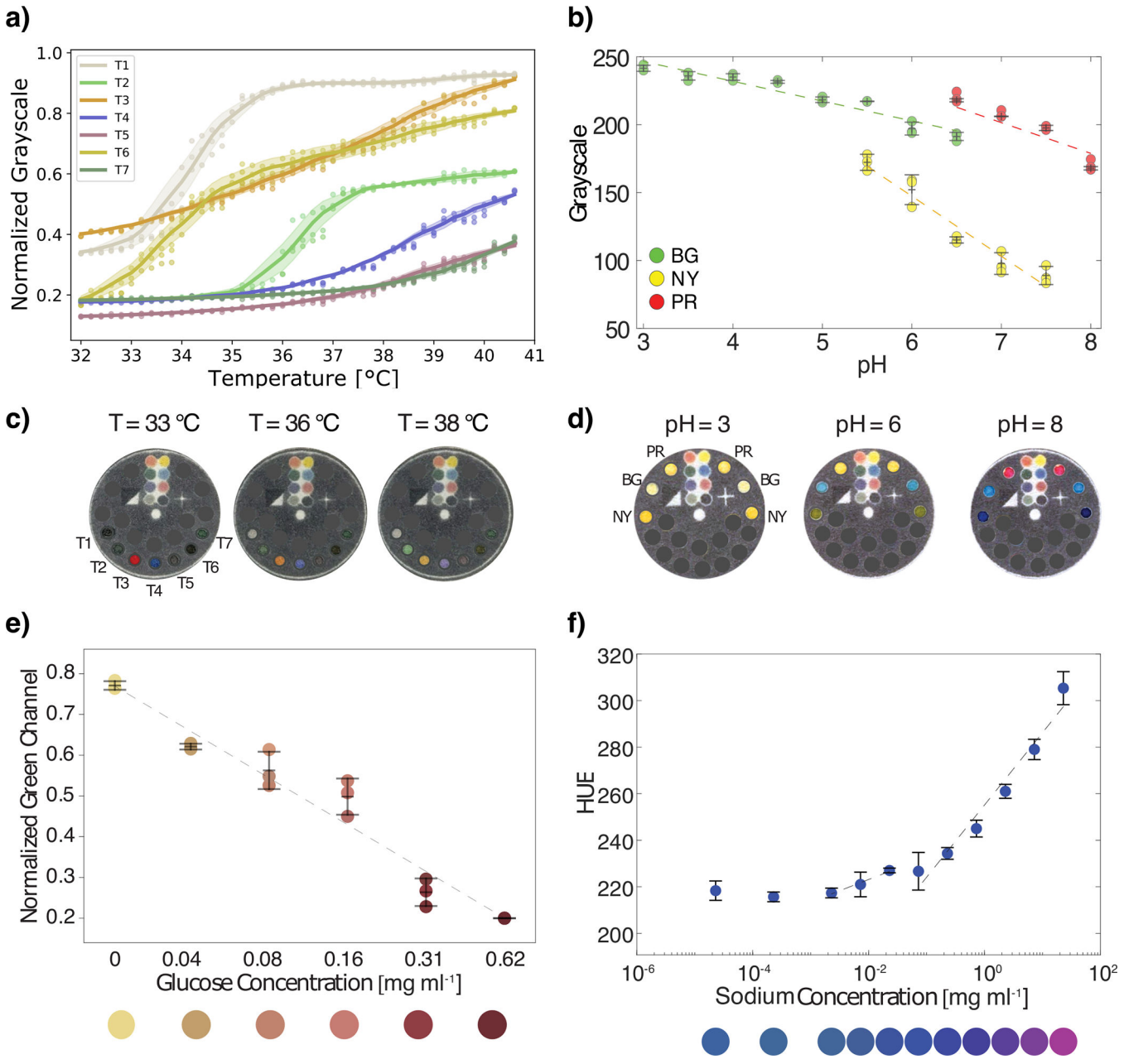

Figure 2. (A) Temperature colorimetric dye responses in the range 32 °C to 41 °C. (B) Colorimetric dye responses in the pH range 3 to 8. (C) Experimental sensor images for temperature at 33 °C, 36 °C, and 38 °C. (D) Experimental sensor images for pH at 3, 6, and 8. (E) Glucose colorimetric dye response in the sensing range 0.039−0.625 mg/mL, with color scale in the bottom. (F) Sodium colorimetric dye response in the sensing range 2.90−29.0 mg/mL, with color scale in the bottom.

the maximum standard deviation (SD) in the grayscale response [0−1] for each dye was: T1 (0.068), T2 (0.055), T3 (0.023), T4 (0.020), T5 (0.012), T6 (0.032), T7 (0.014).

Colorimetric measurements of *pH* were performed via three different sensing dyes (PR, BG, NY), each exhibiting a unique colorimetric response in the pH range from 3 to 8.5 (Figure 2b,d; Figure S2b), with the respective sensitivities (normalized (norm.) grayscale/pH) and pH sensing ranges of: PR (−0.073, 6.5−8.5), BG (−0.094, 3−6.5) and NY(−0.117, 5.5−7.5), with a maximum grayscale SD of: PR (0.048), BG (0.065) and NY (0.016), demonstrating viability within the relevant pH range for clinical applications.

Characterization of the *glucose* colorimetric dye showed a sensitivity of −1.95 (norm. green-channel/mg mL^{-1}) with a sensing range from 0.039 mg mL^{-1} to 0.625 mg mL^{-1}, while the maximum SD of the green-channel intensity for three replicates was 0.081 (Figure 2e).

The *sodium* colorimetric dye displayed a sensitivity of 0.014 (norm. red-channel/mg mL^{-1}) and 2.81 (hue/mg mL^{-1}) in the sensing range of 2.92 mg mL^{-1}(0.05 mol L^{-1} NaCl) to 29.20 mg mL^{-1} (0.5 mol L^{-1} of NaCl), with a maximum SD of the red-channel intensity of 0.075 (Figure 2f).

The temperature colorimetric response was further examined by exposing the sensors to continuous temperature cyclic variations in the measurement range. All the temperature dyes (T1−T6) showed cyclic, i.e., bidirectional reversible color responses (Figure S4a), and hysteresis was bound below 0.025 in the normalized grayscale [0−1], equivalent to 0.78 °C for the T3 dye.

https://doi.org/10.1021/acssensors.5c04171
ACS Sens. XXXX, XXX, XXX-XXX

For the pH dyes (PR, BG, NY) cyclic color changes were observed in a laboratory set-up with continuous exposure to a changing pH solution, grayscale [0−1] hysteresis for the pH dyes was PR (0.065 ± 0.026), BG (0.103 ± 0.064) and NY (0.112 ± 0.055; average ± SD), equivalent to 0.55 pH units for the PR dye (Figure S4b).

For the pH and sodium inks, reversibility depends on their binding equilibrium, and further evaluation in complex environments is required.[35] In contrast, glucose-responsive dyes enable one-way measurement by undergoing a binding-induced signal change that reaches saturation.

Unlike many conventional detection agents, silk-based materials are chemically stable and do not undergo nonspecific redox reactions under regular operating conditions. Therefore, long-term storage stability and retained colorimetric response in pH, temperature, and glucose have been previously proven for silk-fibroin supported dyes for 24 months under refrigerated conditions (4 °C), and 2.5 months for pH and temperature in accelerated aging conditions (60 °C),[21,35] and at least 8 days for glucose at (25 °C).[36]

The multichannel colorimetric design enhances readout robustness by mitigating classical selectivity and interference limitations in complex biofluids. Chemical interference and selectivity toward common biofluid components, including lactate and ascorbic acid, have been extensively evaluated in our prior work, both with and without *de novo* proteins, demonstrating minimal cross-reactivity and preserved analytical performance.[37]

Automated AI-Supported Colorimetric Measurement

Parameter regression in the sensing ranges of each dye was achieved with high precision by the U-Net denoising models for: Temperature (Mean absolute error (MAE) = 0.455 °C, Spearman Rank correlation $\rho = 0.968$, p-value = 3.23×10^{-133}); pH (MAE = 0.416, $\rho = 0.967$, p-value = 2.56×10^{-143}); Sodium (MAE = 0.857 mg/mL, $\rho = 0.965$, p-value = 6.49×10^{-140}); and Glucose (MAE = 0.0187 mg/mL, $\rho = 0.982$, p-value = 1.83×10^{-173}) (Table 1, Figure S3a); requiring 0.151 ± 0.015 s per image (CPU Apple M1, 16GB RAM) under neutral white light, with added sensor shear/rotation and an image resolution of 128 × 128 pixels. The U-Net denoising model performed comparably to the baseline for pH, but significantly reduced prediction errors for temperature (Mann-Whitney U Test, U = 39419, p-value = 1.736×10^{-6}), sodium (U = 36216.5, p-value = 2.852×10^{-4}), and glucose (U = 48461.5, p-value = 4.9×10^{-29}) (Table 1, Figure S3b).

In addition, the model's ability to detect clinically relevant pathological thresholds in neonatal interstitial fluid was assessed. The model demonstrated high balanced accuracy (b.acc.) and weighted (w.) F1-scores in identifying critical thresholds for cystic fibrosis (b.acc. 91.40%, w.F1 93.19%) for sodium above 2.0 mg/mL;[38] hypernatremia (b.acc. 92.52%, w.F1 90.95%) for sodium above 3.5 mg/mL;[39] hypoglycemia (b.acc. 98.08%, w.F1 99.16%) for glucose below 0.5 mg/mL;[4,6] pH imbalances, with identification of pH above 7.5 (b.acc. 93.36%, w.F1 95.77%,) and pH below 7 (b.acc. 92.99%, w.F1 94.10%), for a healthy pH range of 7.30−7.45;[40] and thermal dysregulation with hyperthermia (b.acc. 96.58%, w.F1 97.15%) and hypothermia (b.acc. 98.11%, w.F1 98.17%) when outside the 36.5−37.5 °C range[41] (see confusion matrices Figure S1).

The U-Net denoising model maintained high colorimetric prediction accuracy in challenging illumination conditions, including random color illumination shifts and nonuniform spatial perturbation at 10% and 20% noise (Table 1). Even at a noise level of 20%, predictions remained robust (Figure 3b): for Temperature (MAE = 0.479 °C, $\rho = 0.9562$ p-value = 1.31×10^{-129}), pH (MAE = 0.467, $\rho = 0.9564$ p-value = 2.93×10^{-129}), Sodium (MAE = 0.848 mg/mL, $\rho = 0.966$ p-value = 3.10×10^{-141}), and Glucose (MAE = 0.0224 mg/mL, $\rho = 0.964$ p-value = 7.18×10^{-139}). Relative to white-light conditions, performance differences were minimal, with mean error changes of temperature (0.0381, 95% confidence Interval (CI): -9.36×10^{-5} to 0.0764), pH (0.0729, 95% CI: 0.0187 to 0.127), sodium (0.0582, 95% CI: -1.864×10^{-5} to 0.116), glucose (0.00672, 95% CI: 9.18×10^{-4} to 0.0125), demonstrating resilience to complex illumination artifacts and image shear/rotations.

In contrast to the denoising U-Net, two-step baseline methods that first apply a global color correction to the sensor image, based on the color checker references, and a subsequent color regression, have shown decreased performance,[31] as they only estimated a global color homography and can therefore not correct for spatial nonuniform illuminations.[42,43]

Adaptation of the Colorimetric Sensor to Clinically Relevant Conditions

Microfluidic Evaluation. The sensor's design was optimized for microfluidic performance using capillary effects, enabling the simultaneous contact of multiple dyes with highly comparable fractions of perspiration fluid, while minimizing contact of the sensing dye areas with the skin. Starting from the sole bottom inlet, the fluid effectively reaches the sensing areas through a capillary net that holds 35 μL (Figure 1b). This renders the sensor's design clinically applicable, as the transepidermal fluid loss rate for preterm neonates[13] varies between 15 and 22 g/m^2/h, resulting in a transepidermal sample volume of 23.8−34.8 μL (i.e., 2.1−3.2 μL per sensing area, for n = 11) extrapolation of 38 min, for a Tegaderm patch area of 5x5cm. In the experimental setting, we successfully showed effective colorimetric dye response using small sample volumes between 1 and 3 μL per sensing area for pH, glucose, and sodium.

Dye Stability under Clinical Conditions. Neonatal incubators provide a controlled environment to support critical body functions in the neonate through elevated temperature and humidity. We re-evaluated the performance of the colorimetric sensors inside the incubator (Figure S8d), with 60−80% humidity and with temperature increasing from 34 to 39 °C, successfully demonstrating preservation of the pH dye color saturation after 120 min, comparing a set of two sensors protected by medical water-proof film, against two sensors without the water-proof film. The average pH color saturation after 120 min was higher for the film-covered dyes (PR = 67.1%, BG = 81.2%, NY = 25.0%), and lower without the impermeable film (PR = 46.3%, BG = 64.8%, NY = 15.4%).

Skin Conformability. The use of flexible materials for the sensor (i.e., filter silk paper in combination with 3M Tegaderm) optimized skin contact of the sensor, enabling conformance to body curvature, while avoiding skin traction (Figure 1b).

Automated Sensor Detection in the Neonatal Incubator

Detection and segmentation of the colorimetric sensor in a pilot video dataset acquired in a neonatal incubator demonstrated robust performance across a range of clinically relevant recording conditions. Overall detection accuracy was high across most scenarios (patient movement, low illumination, reflections, unseen camera viewpoints; AP@IoU = 0.50: 0.983−1.000; AP@IoU = 0.75: 0.880−1.000; Figure 1c;Table S6), indicating good generalization to dynamic and visually challenging NICU environments. The most challenging condition was partial obstruction of

https://doi.org/10.1021/acssensors.5c04171
ACS Sens. XXXX, XXX, XXX-XXX

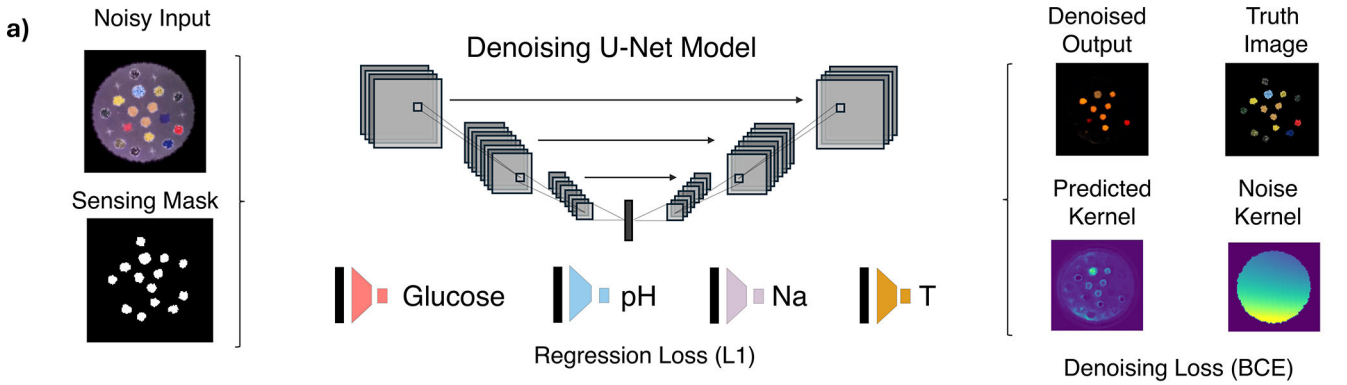

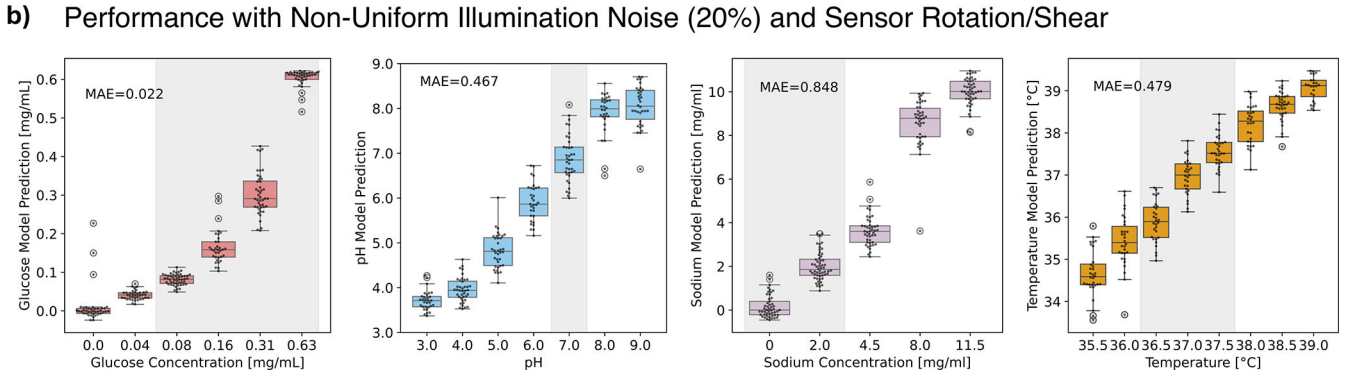

Figure 3. Deep learning model for colorimetric image-based parameter prediction. (A) The model integrates a U-Net denoising architecture and a multilayer perceptron (MLP) to perform regression from the latent embeddings. The multitask loss is formulated as the addition of the denoising loss (binary cross entropy (BCE)) for every color channel and predicted illumination gradient (noise kernel), as well as the regression loss between the predicted value and the true label (L1). (B) Model prediction performance for every parameter, with median and interquartile ranges (IQR) per label. Predictions were performed under random nonuniform illumination noise at max. 20% intensity, with random image shear, rotation, and cropping. Input image size was 128 × 128 pixels. Shaded areas on each plot correspond to estimated clinically relevant thresholds for interstitial fluid (see Table S1).

the sensor by silver-colored electrode cables, which affected the performance noticeably (AP@IoU = 0.50: 0.925; AP@IoU = 0.75: 0.730), since the cables resembled the sensor background, they were assigned to the sensor mask.

Pilot Evaluation in Human Biofluid Samples

Glucose and pH sensor performance was evaluated in noninvasively collected adult saliva and perspiration samples under fasting, post-exercise, and 10 and 25 min postprandial conditions, with parallel validation by ELISA, capillary blood glucose, and laboratory pH measurements.

In saliva, the colorimetric sensor detected a modest glucose increase from fasting to exercise (4.2%, min−max scaled; medians <0.003 mg/mL), consistent with trends observed in ELISA (2.3%; 0.018 to 0.021 mg/mL), and a postprandial rise at 10 min (6.0%), observed with greater magnitude in the ELISA trends (42.9%). At 25 min postprandial, median salivary glucose concentrations were closely matched between the colorimetric sensor (0.076 mg/mL, interquartile range (IQR): 0.055−0.110) and ELISA (0.073 mg/mL, IQR: 0.045−0.101), with baseline increments of 43.8% and 48.9%, respectively. In perspiration, glucose levels remained low (<0.004 mg/mL), consistent with ELISA (0.018 mg/mL). Capillary blood glucose increased from 0.86 mg/mL (fasting) to 0.96 mg/mL (post-exercise), as well as 0.87 mg/mL and 1.01 mg/mL for 10min and 25min postprandial, respectively, confirming systemic glycemic trends (Figure 4a).

Table 1. Colorimetric Reading Model Performance with Image Shear/Rotation and Illumination Noise[a]

noise [%]	model	temperature [°C]	pH	sodium [mg/mL]	glucose [mg/mL]
0	baseline	0.582 ± 0.348	0.413 ± 0.273	1.279 ± 1.210	0.050 ± 0.041
0	U-Net	0.455 ± 0.379	0.416 ± 0.356	0.857 ± 0.701	0.019 ± 0.026
10	U-Net	0.519 ± 0.384	0.426 ± 0.338	0.847 ± 0.748	0.020 ± 0.024
20	U-Net	0.479 ± 0.397	0.467 ± 0.376	0.848 ± 0.672	0.022 ± 0.029

[a]Noise refers to the maximum intensity of the nonuniform illumination. Mean absolute error (MAE) and its standard deviation (±) were estimated with a test set (N = 240) per variable. All images are sampled from experimental data and augmented by applying shear and rotations to the sensor image, with different levels of illumination noise. The temperature range was evaluated from 35.5−39 °C, as shown in Figure 3b.

https://doi.org/10.1021/acssensors.5c04171
ACS Sens. XXXX, XXX, XXX-XXX

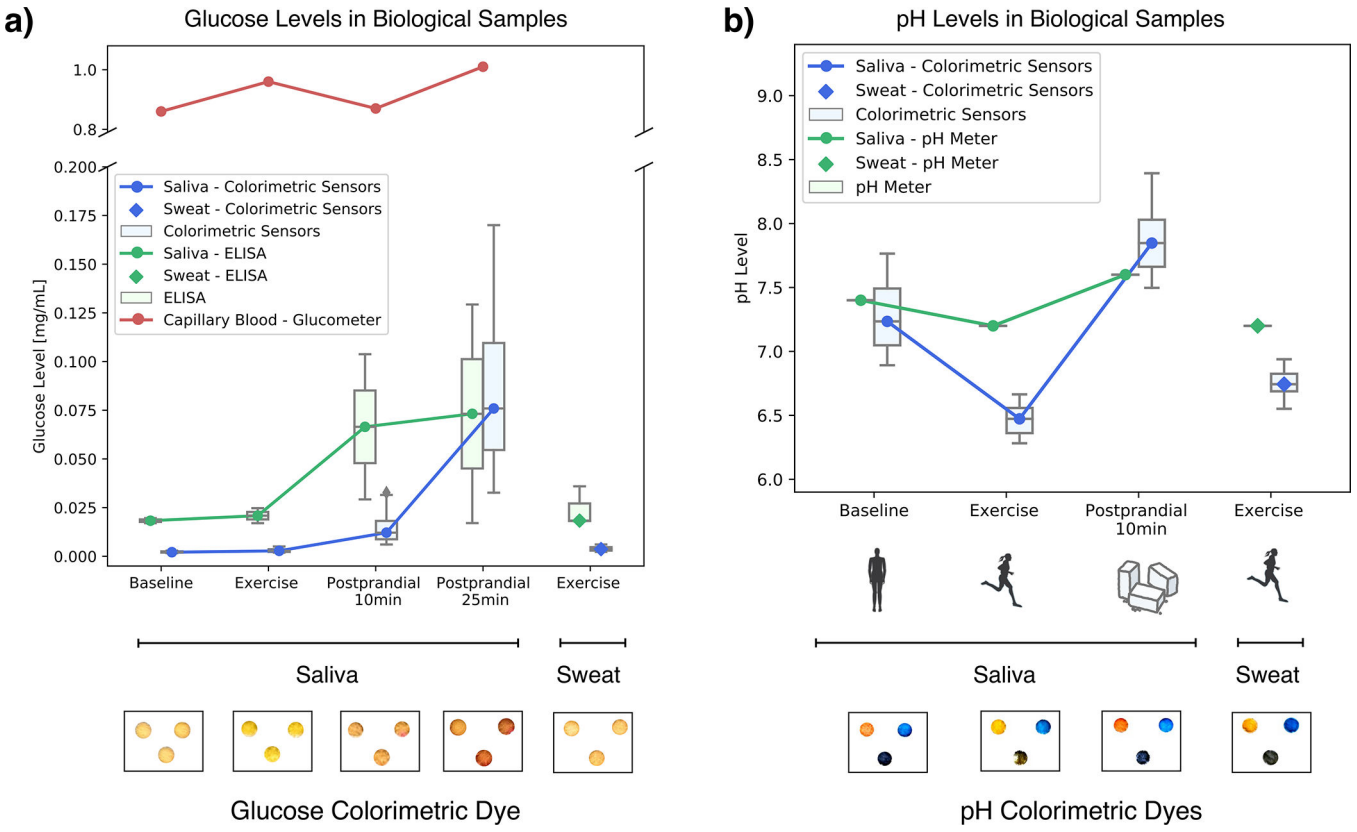

Figure 4. Pilot evaluation of the multibiomarker colorimetric sensor in saliva and perspiration samples under three physiological conditions: a fasting baseline, after exercise, and postprandial. (A) Glucose measurement by the colorimetric sensor, validated by parallel ELISA test and capillary blood glucose measurements. The bottom row shows experimental images of the glucose colorimetric response. (B) pH measurement by the colorimetric sensor, validated in parallel by a laboratory pH-meter. The bottom row shows experimental images of the pH colorimetric response (left = PR, right = BG, bottom = NY).

Salivary pH decreased from fasting to exercise, with the colorimetric sensor capturing a 36% reduction (median 7.24 (IQR: 7.05−7.49) to 6.47 (IQR: 6.36−6.56)), compared with a larger 50% decrease measured by the pH meter (7.40 to 7.20). Postprandially, both methods detected pH elevation relative to fasting, with the sensor reporting a 29% increase (median 7.85; IQR: 7.66−8.03) and the pH meter a 50% increase (7.60), indicating concordant directional and relative magnitude changes despite systematic scale differences (Figure 4b).

Pixel-wise experimental color distributions for both glucose and pH differed significantly across all physiological conditions (Kruskal-Wallis, H = 5392.224, p-value < 0.001), with post-hoc tests confirming differences between fasting, exercise, and postprandial states (Mann-Whitney U, adj. p-value < 0.001, respectively; Supporting Information, Statistical Analysis).

DISCUSSION

We showcased novel shelf-stable colorimetric sensing patches in a proof-of-principle study for automated noninvasive monitoring of critical body function biomarkers in neonates, via perspiration or saliva. The sensor's optimized design leverages the ability of silk fibroin to stabilize labile molecules, realizing multiple dyes on a miniaturized patch with a skin-friendly bottom sample inlet, and catering to the clinical requirements of a sensitive patient population. Automated quantification of the colorimetric response via deep learning models provided accurate and robust measurements in relevant ranges and under critical clinical conditions, such as image perspective shear/rotation, uncontrolled light, and enabled sensor tracking on a moving object, key requirements for their implementation as a wearable monitoring technology in the neonatal incubator. Functionality with biological fluids was successfully demonstrated in an experimental setting with different physiological conditions.

The colorimetric dyes showed high sensitivity for parameter measurement in ranges relevant in neonatal care (Figure 2), and robustness to various sources of variability (i.e., pixel-wise color distributions per dye, inter-sensor variability, and model prediction uncertainty), indicating the potential for clinical use to identify critical physiological events (e.g., metabolic acidosis/alkalosis, glycemia, cystic fibrosis).[44] The microfluidic design for passive perspiration sample collection enables multiarray sensing holding a total volume of 35 μL (for 11 sensing areas), realizing measurements in samples as small as 3 μL per sensing area. The sample volume is comparable to the requirements of clinical iontophoresis in infants (>18 μL in 30 min),[10] while matching the natural rate of transepidermal fluid loss of preterm neonates in 15−40 min.[13] The sensor thereby reaches a milestone in catering to the demand of smaller sample volumes than alternative devices for passive adult perspiration collection (50−100 μL).[17,25,26] Furthermore, the lightweight (0.05g) colorimetric paper sensor patch resulted in a curvilinear, highly conformal water-resistant interface needed for contacting the fragile newborn skin, facilitating the rapid attachment of the

https://doi.org/10.1021/acssensors.5c04171
ACS Sens. XXXX, XXX, XXX-XXX

adhesive patch and amplifying substrate stability in the humid conditions of the neonatal incubator.

As a critical prerequisite for device application in real-life, clinical settings, the deep learning models showed high performance for color-based parameter reading in varied conditions, with accuracy comparable to previously published studies, including sensor shear (acc. 89%)[21] and fixed illumination setups (acc. 99%).[20] Moreover, accurate segmentation of the sensors in videos recorded inside the neonatal incubator was achieved, including high-prevalence conditions such as object movement, varied illumination, and the appearance of occlusion elements, allowing identification of challenging edge cases (e.g., silver-colored electrodes) for future model fine-tuning. Conditions of the daily clinical workflow can critically limit the technology performance, as observed in studies using computer vision models in the neonatal intensive care unit (NICU),[45] and therefore require extensive evaluation for transition into the clinic.

The deep-learning readout models can be readily adapted to new sensor designs requiring only the sensor mask and representative color distributions, making the workflow robust to future sensor iterations. Likewise, the image augmentation strategy, accounting for shear and uneven illumination, is transferable to other point-of-care imaging applications with uncontrolled lighting.

Pilot validation measurements in biological fluids captured pre- and post-prandial glucose dynamics as well as exercise-induced pH changes, demonstrating the capacity of the colorimetric sensor to respond to physiologically relevant variations under real-world conditions. The concordant trends observed between perspiration fluid and capillary blood measurements highlight the potential of noninvasive biofluids to inform timely clinical decision-making. However, owing to the single-subject, proof-of-concept nature of these experiments, the results should be interpreted as qualitative evidence of the sensor's ability to detect differential physiological trends rather than as an assessment of quantitative clinical accuracy. Comprehensive validation in larger cohorts and across diverse biological matrices will be required to establish robustness, matrix effects, and clinical performance. In previous studies, a close relation of changes in biomarkers from saliva, perspiration, or interstitial fluid, and systemic changes in the blood have been observed, with specific examples for glucose, pH, electrolytes,[10,40,46,47] and successful applications in the newborn clinical setting.[4]

Next steps toward clinical implementation will require toxicological safety assessments and prospective studies with paired sampling of transepidermal fluid and capillary blood to establish quantitative correlations between analyte concentrations in both matrices. These studies should include participants across different gestational age groups to account for variation in skin maturity and be conducted under diverse physiological and pathophysiological conditions to improve biomarker interpretability. These investigations will necessitate close collaboration with regulatory authorities and strict adherence to ethical guidelines, given the vulnerability of the neonatal patient population and the limited volumes of blood permissible for sampling. In parallel, further sensor development may include optimizing colorimetric dyes to target additional parameters, such as CO_2 or oxygen saturation, advancing microfluidic designs to enable longitudinal measurements of all analytes, and comprehensively evaluating potential interferents present in neonatal biofluids to strengthen analytical selectivity in future validation phases.

To improve the performance of the deep learning models and enable clinical translation, the image dataset should be expanded to include diverse NICU environments (different incubators, camera angles, and lighting conditions) across multiple centers and patients covering a wide range of skin tones and body types. The proposed deep neural architectures for image-based parameter prediction must also be optimized for settings with limited hardware resources to be deployable on-site.

The advancement of noninvasive monitoring via shelf-stable, paper-based colorimetric disposable sensors optimized for clinical needs in high-end patients, in combination with automated AI-based read-out, holds significant potential for transforming neonatal clinical care. By providing noninvasive monitoring for critical metabolic and respiratory biomarkers through a wearable device in perspiration or saliva, their clinical application will reduce the need for frequent invasive measurements, decrease the incidence of undetected health imbalances, and thereby improve clinical decision-making. The novel medical technology offers a low-cost, easily applicable, miniaturized solution, delivering critical information at the point of care, thereby aligning with the emerging landscape of digital health technologies while expanding access to high-quality care in the neonate. These sensors hold significant promise for future applications in low-resource or underserved settings.

■ ASSOCIATED CONTENT

Supporting Information

The Supporting Information is available free of charge at https://pubs.acs.org/doi/10.1021/acssensors.5c04171.

The data, model weights, and code repository that support the findings of this study are openly available at https://github.com/SchubertLab/biofluid_colorimetric_sensors and in the supplementary material of this article. Detailed method descriptions, additional tables describing targeted biological parameter ranges of the sensor, descriptions of the collected video recordings, hyperparameter grids of the deep learning models, and extended figures illustrating the experimental setups, sensor calibrations, and deep learning pipelines (DOCX)

■ AUTHOR INFORMATION

Corresponding Authors

Benjamin Schubert − *Computational Health Center, Helmholtz Center Munich, Neuherberg 85764 Germany;* orcid.org/0000-0003-3412-1102; Email: Benjamin.schubert@helmholtz-munich.de

Fiorenzo G. Omenetto − *Silklab, Dept. of Biomedical Engineering, Tufts University, Medford, Massachusetts 02155, United States; Dept. of. Electrical and Computer Engineering, Tufts University, Medford, Massachusetts 02155, United States; Dept. Of Physics, Tufts University, Medford, Massachusetts 02155, United States;* orcid.org/0000-0002-0327-853X; Email: Fiorenzo.Omenetto@tufts.edu

Anne Hilgendorff − *Comprehensive Pneumology Center with the CPC-M bioArchive and Institute of Lung Health and Immunity, Helmholtz Center Munich, Munich 81399, Germany; Dr. von Hauner Children's Hospital, Hospital of the Ludwig-Maximilians-Universität München, Munich 80337, Germany; School of Medicine and Health Sciences,*

https://doi.org/10.1021/acssensors.5c04171
ACS Sens. XXXX, XXX, XXX-XXX

Department of Paediatrics, Section of Neonatology, Pediatric Intensive Care, Pediatric Cardiology, Pediatric Pneumology and Allergology and Research Centre Neurosensory Science, Carl von Ossietzky University Oldenburg, Oldenburg 26129, Germany; Email: Anne.hilgendorff@uni-oldenburg.de

Authors

Alejandra Castelblanco – *Computational Health Center, Helmholtz Center Munich, Neuherberg 85764 Germany; School of Computation, Information and Technology, Technical University of Munich, Munich 85748 Germany;* orcid.org/0000-0002-1147-758X

Elisabetta Ruggeri – *Silklab, Dept. of Biomedical Engineering, Tufts University, Medford, Massachusetts 02155, United States*

Giusy Matzeu – *Silklab, Dept. of Biomedical Engineering, Tufts University, Medford, Massachusetts 02155, United States*

Motaharehsadat Heydarian – *Comprehensive Pneumology Center with the CPC-M bioArchive and Institute of Lung Health and Immunity, Helmholtz Center Munich, Munich 81399, Germany*

Kai Foerster – *Comprehensive Pneumology Center with the CPC-M bioArchive and Institute of Lung Health and Immunity, Helmholtz Center Munich, Munich 81399, Germany; Dr. von Hauner Children's Hospital, Hospital of the Ludwig-Maximilians-Universität München, Munich 80337, Germany*

Ahmed Bahnasy – *School of Computation, Information and Technology, Technical University of Munich, Munich 85748 Germany*

Andreas Flemmer – *Dr. von Hauner Children's Hospital, Hospital of the Ludwig-Maximilians-Universität München, Munich 80337, Germany*

Julia A. Schnabel – *Computational Health Center, Helmholtz Center Munich, Neuherberg 85764 Germany; School of Computation, Information and Technology, Technical University of Munich, Munich 85748 Germany; School of Biomedical Engineering and Imaging Sciences, King's College London, London WC2R 2LS, U.K.*

Complete contact information is available at: https://pubs.acs.org/doi/10.1021/acssensors.5c04171

Author Contributions

†A.C. and E.R. contributed equally to this work.

Notes

The authors declare no competing financial interest.

■ ACKNOWLEDGMENTS

The present study was supported by the Young Investigator Grant NWG VH-NG-829 (Helmholtz Association), Federal Ministry of Education and Research in Germany (BMBF), Helmholtz Munich, Germany, and the German Centre for Lung Research (DZL) (BMBF). The present study is part of the transregional collaborative research center PILOT (TRR 359 Perinatal Development of Immune Cell Topology, Project number 491676693) funded through the Deutsche Forschungsgemeinschaft (DFG, German Research Foundation). A.C. is supported by the Helmholtz Association under the research school Munich School for Data Science. Computational resources for deep learning model training were supported by the BMBF-funded de.NBI Cloud within the German Network for Bioinformatics Infrastructure (de.NBI). Additional financial support was provided by the Stiftung AtemWeg (LSS AIRR).

A preprint of this article was posted on *medRxiv*: Castelblanco, A.; Ruggeri, E.; Matzeu, G.; Heydarian, M.; Foerster, K.; Bahnasy, A.; Flemmer, A.; Schnabel, J.; Schubert, B.; Omenetto, F.; Hilgendorff, A Wireless Colorimetric Multibiomarker Sensing to Enable Critical Neonatal Monitoring. *medRxiv*, 2025. DOI:10.1101/2025.09.21.25336258 (Published September 22, 2025).

■ REFERENCES

(1) Lorenz, J. M. Fluid and Electrolyte Therapy in the Very Low-Birthweight Neonate. *Neoreviews* **2008**, *9* (3), e102–e108.

(2) Hillman, N.; Kallapur, S. G.; Jobe, A. Physiology of Transition from Intrauterine to Extrauterine Life, Clin. *Clin. Perinatol.* **2012**, *39* (4), 769–783.

(3) Baumeister, F. A. M.; Rolinski, B.; Busch, R.; Emmrich, P. Glucose Monitoring with Long-Term Subcutaneous Microdialysis in Neonates. *Pediatrics* **2001**, *108* (5), 1187–1192.

(4) Beardsall, K.; Thompson, L.; Guy, C.; Bond, S.; Allison, A.; Pantaleo, B.; Petrou, S.; Kim, S.; Dunger, D.; Hovorka, R. Continuous Glucose Monitoring in Extremely Preterm Infants in Intensive Care: The REACT RCT and Pilot Study of "closed-Loop" Technology. *Efficacy Mech. Eval.* **2021**, *8* (16), 1–142.

(5) Choi, H.-Y.; Corder, W.; Tefera, E.; Abubakar, K. M. Comparison of Point-of-Care versus Central Laboratory Testing of Electrolytes, Hemoglobin, and Bilirubin in Neonates. *Am. J. Perinatol.* **2022**, *39* (16), 1786–1791.

(6) Harris, D. L.; Battin, M. R.; Weston, P. J.; Harding, J. E.; Continuous Glucose Monitoring in Newborn Babies at Risk of Hypoglycemia. *J. Pediatr.* **2010**, *157* (2), 198–202.

(7) Southern, K. W.; Munck, A.; Pollitt, R.; Travert, G.; Zanolla, L.; Dankert-Roelse, J.; Castellani, C. A Survey of Newborn Screening for Cystic Fibrosis in Europe. *J. Cyst. Fibros.* **2007**, *6* (1), 57–65.

(8) Chung, H. U.; Kim, B. H.; Lee, J. Y.; Lee, J.; Xie, Z.; Ibler, E. M.; Lee, K.; Banks, A.; Jeong, J. Y.; Kim, J.; Ogle, C.; Grande, D.; Yu, Y.; Jang, H.; Assem, P.; Ryu, D.; Kwak, J. W.; Namkoong, M.; Park, J. B.; Lee, Y.; Kim, D. H.; Ryu, A.; Jeong, J.; You, K.; Ji, B.; Liu, Z.; Huo, Q.; Feng, X.; Deng, Y.; Xu, Y.; Jang, K.-I.; Kim, J.; Zhang, Y.; Ghaffari, R.; Rand, C. M.; Schau, M.; Hamvas, A.; Weese-Mayer, D. E.; Huang, Y.; Lee, S. M.; Lee, C. H.; Shanbhag, N. R.; Paller, A. S.; Xu, S.; Rogers, J. A. Binodal, Wireless Epidermal Electronic Systems with in-Sensor Analytics for Neonatal Intensive Care. *Science* **2019**, *363* (6430), No. eaau0780.

(9) Hillman, N. H.; Kallapur, S. G.; Jobe, A. H. Physiology of Transition from Intrauterine to Extrauterine Life. *Clin. Perinatol.* **2012**, *39* (4), 769–783.

(10) LeGrys, V. A.; Yankaskas, J. R.; Quittell, L. M.; Marshall, B. C.; Mogayzel, P. J. Jr. Cystic Fibrosis Foundation. Diagnostic Sweat Testing: The Cystic Fibrosis Foundation Guidelines. *J. Pediatr.* **2007**, *151* (1), 85–89.

(11) Mckinlay, C. J. D.; Chase, J.; Dickson, J.; Harris, D. L.; Alsweiler, J. M.; Harding, J. E. Continuous Glucose Monitoring in Neonates: A Review, Maternal Health. *Neonatol. Perinatol.* **2017**, *3* (1), No. 18.

(12) Oh, W. Fluid and Electrolyte Management of Very Low Birth Weight Infants. *Pediatr. Neonatol.* **2012**, *53* (6), 329–333.

(13) Mathanda, T. R.; M. Bhat, R.; Hegde, P.; Anand, S. Transepidermal Water Loss in Neonates: Baseline Values Using a Closed-Chamber System. *Pediatr. Dermatol.* **2016**, *33* (1), 33–37.

(14) Sempionatto, J. R.; Lin, M.; Yin, L.; De la paz, E.; Pei, K.; Sonsa-ard, T.; de Loyola Silva, A. N.; Khorshed, A. A.; Zhang, F.; Tostado, N.; Xu, S.; Wang, J. An Epidermal Patch for the Simultaneous Monitoring of Haemodynamic and Metabolic Biomarkers. *Nat. Biomed. Eng.* **2021**, *5* (7), 737–748.

(15) Lee, H.; Song, C.; Hong, Y. S.; Kim, M.; Cho, H. R.; Kang, T.; Shin, K.; Choi, S. H.; Hyeon, T.; Kim, D.-H. Wearable/disposable Sweat-Based Glucose Monitoring Device with Multistage Transdermal Drug Delivery Module. *Sci. Adv.* **2017**, *3* (3), No. e1601314.
(16) Wang, J.; Luo, Y.; Zhou, Z.; Xiao, J.; Xu, T.; Zhang, X. Epidermal Wearable Optical Sensors for Sweat Monitoring. *Commun. Mater.* **2024**, *5* (1), No. 77.
(17) Wu, C.-H.; Ma, H. J. H.; Baessler, P.; Balanay, R. K.; Ray, T. R. Skin-Interfaced Microfluidic Systems with Spatially Engineered 3D Fluidics for Sweat Capture and Analysis. *Sci. Adv.* **2023**, *9* (18), No. eadg4272.
(18) Terse-Thakoor, T.; Punjiya, M.; Matharu, Z.; Lyu, B.; Ahmad, M.; Giles, G. E.; Owyeung, R.; Alaimo, F.; Shojaei Baghini, M.; Brunyé, T. T.; Sonkusale, S. Thread-Based Multiplexed Sensor Patch for Real-Time Sweat Monitoring. *npj Flexible Electron.* **2020**, *4* (1), No. 18.
(19) Krishnan, S.; Syed, Z. U. Q. Colorimetric Visual Sensors for Point-of-Needs Testing. *Sensors Actuators Rep.* **2022**, *4* (2), No. 100078.
(20) Rahman, M. M.; Uddin, M. J.; Hong, J. H.; Bhuiyan, N. H.; Shim, J. S. Lab-in-a-Cup (LiC): An Autonomous Fluidic Device for Daily Urinalysis Using Smartphone. *Sens. Actuators B* **2022**, *355*, No. 131336.
(21) Ruggeri, E.; Matzeu, G.; Vergine, A.; De Nicolao, G.; Omenetto, F. G. Paper-based Wearable Patches for Real-time, Quantitative Lactate Monitoring. *Adv. Sens. Res.* **2024**, *3* (2), No. 2300141.
(22) Matzeu, G.; Naveh, G. R. S.; Agarwal, S.; Roshko, J. A.; Ostrovsky-Snider, N. A.; Napier, B. S.; Omenetto, F. G. Functionalized Mouth-Conformable Interfaces for pH Evaluation of the Oral Cavity. *Adv. Sci.* **2021**, *8* (12), No. e2003416.
(23) Zheng, X. T.; Goh, W. P.; Yu, Y.; Sutarlie, L.; Chen, D. Y.; Tan, S. C. L.; Jiang, C.; Zhao, M.; Ba, T.; Li, H.; Su, X.; Yang, L. Skin-Attachable Ink-Dispenser-Printed Paper Fluidic Sensor Patch for Colorimetric Sweat Analysis. *Adv. Healthcare Mater.* **2024**, *13* (3), No. e2302173.
(24) Gao, Y.; Choi, S. Micropatternable Janus Paper as a Wearable Skin Patch for Sweat Collection and Analysis. *Adv. Mater. Technol.* **2023**, *8* (17), No. 2300396.
(25) Wang, L.; Xu, T.; He, X.; Zhang, X. Flexible, Self-Healable, Adhesive and Wearable Hydrogel Patch for Colorimetric Sweat Detection. *J. Mater. Chem. C* **2021**, *9* (41), 14938–14945.
(26) Baker, L. B.; Model, J. B.; Barnes, K. A.; Anderson, M. L.; Lee, S. P.; Lee, K. A.; Brown, S. D.; Reimel, A. J.; Roberts, T. J.; Nuccio, R. P.; Bonsignore, J. L.; Ungaro, C. T.; Carter, J. M.; Li, W.; Seib, M. S.; Reeder, J. T.; Aranyosi, A. J.; Rogers, J. A.; Ghaffari, R. Skin-Interfaced Microfluidic System with Personalized Sweating Rate and Sweat Chloride Analytics for Sports Science Applications. *Sci. Adv.* **2020**, *6* (50), No. eabe3929.
(27) Cho, S.; Shaban, S. M.; Song, R.; Zhang, H.; Yang, D.; Kim, M.-J.; Xiong, Y.; Li, X.; Madsen, K.; Wapnick, S.; Zhang, S.; Chen, Z.; Kim, J.; Guinto, G.; Li, M.; Lee, M.; Nuxoll, R. F.; Shajari, S.; Wang, J.; Son, S.; Shin, J.; Aranyosi, A. J.; Wright, D. E.; Kim, T.-I.; Ghaffari, R.; Huang, Y.; Kim, D.-H.; Rogers, J. A. A Skin-Interfaced Microfluidic Platform Supports Dynamic Sweat Biochemical Analysis during Human Exercise. *Sci. Transl. Med.* **2024**, *16* (763), No. eado5366.
(28) Akyazi, T.; Basabe-Desmonts, L.; Benito-Lopez, F. Review on Microfluidic Paper-Based Analytical Devices towards Commercialisation. *Anal. Chim. Acta* **2018**, *1001*, 1–17.
(29) Carrell, C.; Kava, A.; Nguyen, M.; Menger, R.; Munshi, Z.; Call, Z.; Nussbaum, M.; Henry, C. Beyond the Lateral Flow Assay: A Review of Paper-Based Microfluidics. *Microelectron. Eng.* **2019**, *206*, 45–54.
(30) Ra, M.; Muhammad, M. S.; Lim, C.; Han, S.; Jung, C.; Kim, W. Y. Smartphone-Based Point-of-Care Urinalysis under Variable Illumination. *IEEE J. Transl. Eng. Health Med.* **2018**, *6*, 1–11.
(31) Castelblanco, A.; Matzeu, G.; Ruggeri, E.; Omenetto, F. G.; Hilgendorff, A.; Schnabel, J. A.; Schubert, B. Colorimetric Sensor Reading and Illumination Correction via Multi-Task Deep-Learning. *IEEE Eng. Med. Biol. Soc.* **2023**, *2023*, 1–5.
(32) Ronneberger, O.; Fischer, P.; Brox, T.; Navab, N.; Hornegger, J.; Wells, W. M.; Frangi, A. F. U-Net: Convolutional Networks for Biomedical Image Segmentation. *Int. Conf. Med. Image Comput. Comput.-Assisted Intervention* **2015**, *9351*, 234–241.
(33) He, K.; Gkioxari, G.; Dollár, P.; Girshick, R. Mask R-CNN. In *2017 IEEE International Conference on Computer Vision (ICCV)*. https://ieeexplore.ieee.org/document/823758zxcz4. DOI: 10.1109/ICCV.2017.322 (accessed 2025-04-07).
(34) Russell, B. C.; Torralba, A.; Murphy, K. P.; Freeman, W. T. LabelMe: A Database and Web-Based Tool for Image Annotation. *Int. J. Comput. Vision* **2007**, *77* (1), 157–173.
(35) Matzeu, G.; Mogas-Soldevila, L.; Li, W.; Naidu, A.; Turner, T. H.; Gu, R.; Blumeris, P. R.; Song, P.; Pascal, D. G.; Guidetti, G.; Li, M.; Omenetto, F. G. Large-Scale Patterning of Reactive Surfaces for Wearable and Environmentally Deployable Sensors. *Adv. Mater.* **2020**, *32* (28), No. e2001258.
(36) Tao, H.; Marelli, B.; Yang, M.; An, B.; Onses, M. S.; Rogers, J. A.; Kaplan, D. L.; Omenetto, F. G. Inkjet Printing of Regenerated Silk Fibroin: From Printable Forms to Printable Functions. *Adv. Mater.* **2015**, *27* (29), 4273–4279.
(37) d'Amone, L.; Matzeu, G.; Quijano-Rubio, A.; Callahan, G. P.; Napier, B.; Baker, D.; Omenetto, F. G. Reshaping de Novo Protein Switches into Bioresponsive Materials for Biomarker, Toxin, and Viral Detection. *Adv. Mater.* **2023**, *35* (11), No. e2208556.
(38) Gonçalves, A. C.; Marson, F. A. L.; Mendonça, R. M. H.; Bertuzzo, C. S.; Paschoal, I. A.; Ribeiro, J. D.; Ribeiro, A. F.; Levy, C. E. Chloride and Sodium Ion Concentrations in Saliva and Sweat as a Method to Diagnose Cystic Fibrosis. *J. Pediatria* **2019**, *95* (4), 443–450.
(39) Bhatia, J. Fluid and Electrolyte Management in the Very Low Birth Weight Neonate. *J. Perinatology* **2006**, *26* (1), S19–S21.
(40) Hussain, N. M.; Amin, B.; O'Halloran, M.; Elahi, A. Development and Characterization of Interstitial-Fluid-Mimicking Solutions for Pre-Clinical Assessment of Hypoxia. *Diagnostics* **2023**, *13* (19), No. 3125.
(41) Knobel, R. B. Thermal Stability of the Premature Infant in Neonatal Intensive Care, Newborn Infant Nurs. *Newborn Infant Nurs. Rev.* **2014**, *14* (2), 72–76.
(42) Finlayson, G.; Gong, H.; Fisher, R. B. Color Homography: Theory and Applications. *IEEE Trans. Pattern Anal. Mach. Intell.* **2019**, *41* (1), 20–33.
(43) Afifi, M.; Price, B.; Cohen, S.; Brown, M. S. When Color Constancy Goes Wrong: Correcting Improperly White-Balanced Images. In *2019 IEEE/CVF Conference on Computer Vision and Pattern Recognition (CVPR)*. **2019**; 1535–1544. DOI: 10.1109/CVPR.2019.00163.
(44) Pullan, N. J.; Thurston, V.; Barber, S. Evaluation of an Inductively Coupled Plasma Mass Spectrometry Method for the Analysis of Sweat Chloride and Sodium for Use in the Diagnosis of Cystic Fibrosis. *Ann. Clin. Biochem.* **2013**, *50* (3), 267–270.
(45) Dosso, Y. S.; Kyrollos, D.; Greenwood, K. J.; Harrold, J.; Green, J. R. NICUface: Robust Neonatal Face Detection in Complex NICU Scenes. *IEEE Access* **2022**, *10*, 62893–62909.
(46) Bruen, D.; Delaney, C.; Florea, L.; Diamond, D. Glucose Sensing for Diabetes Monitoring: Recent Developments. *Sensors* **2017**, *17* (8), No. 1866.
(47) Kadashetti, V.; Baad, R.; Malik, N.; Shivakumar, K. M.; Vibhute, N.; Belgaumi, U.; Gugawad, S.; Pramod, R. C. Glucose Level Estimation in Diabetes Mellitus by Saliva: A Bloodless Revolution. *Rom. J. Intern. Med.* **2015**, *53* (3), 248–252.

https://doi.org/10.1021/acssensors.5c04171
ACS Sens. XXXX, XXX, XXX-XXX